
**Separation Science and Technology**
Publication details, including instructions for authors and subscription information:
http://www.informaworld.com/smpp/title~content=t713708471

# Pinch Field-Flow Fractionation Using Flow Injection Techniques

Martin A. Afromowitz[a]; John E. Samaras[a]
[a] DEPARTMENT OF ELECTRICAL ENGINEERING, UNIVERSITY OF WASHINGTON, WASHINGTON

**To cite this Article** Afromowitz, Martin A. and Samaras, John E.(1989) 'Pinch Field-Flow Fractionation Using Flow Injection Techniques', Separation Science and Technology, 24: 5, 325 — 339
**To link to this Article: DOI:** 10.1080/01496398908049772
**URL:** http://dx.doi.org/10.1080/01496398908049772

SEPARATION SCIENCE AND TECHNOLOGY, 24(5 & 6), pp. 325-339, 1989

# Pinch Field-Flow Fractionation Using Flow Injection Techniques

MARTIN A. AFROMOWITZ and JOHN E. SAMARAS

DEPARTMENT OF ELECTRICAL ENGINEERING
UNIVERSITY OF WASHINGTON, FT-10
SEATTLE, WASHINGTON 98195



**Abstract**

Flow injection techniques have been used almost exclusively for chemical analysis of homogeneous samples. On the other hand, field-flow fractionation is designed to separate phases in a flowing heterogeneous sample through their differing response to applied force fields. In this work we show that controlled phase separation can be achieved and successfully modeled in flow injection systems. The force that separates the phases is generated intrinsically within the flow tube by the inertial effects of the flow itself.

## INTRODUCTION

The ingenious and varied implementations of field-flow fractionation (FFF) introduced by Giddings and his co-workers (*1–4*) have been used to separate particles ranging from submicron up to 100 μm in diameter. In the presence of all but the highest transverse fields, the description of the dynamics of larger particles in Poiseuille flow is very complicated due to the nonlinearity of the Navier-Stokes equation. Low-field steric FFF experimental results deviate from theoretical expectations, and an anomalous retention factor related to velocity-dependent lift forces was invoked (*5*). Recently, however, theoretical studies by McTigue et al. (*6*) succeeded in explaining the nature of the diverse cross-flow forces experienced by rigid particles in plane Poiseuille flow. This recent theory is here applied to particle separation in a Hagen-Poiseuille flow. We show that the intrinsic drag and lift experienced by large particles in low

transverse field environments, such as normal gravitational fields, lead to very efficient fractionation with systems compatible with those used in flow injection analysis (*7*).

## BACKGROUND

The basic approach of field-flow fractionation (FFF) may be summarized as follows: A dilute separable phase flows through a two-dimensional Poiseuille flow channel which features a large aspect ratio to permit use of one-dimensional expressions. A field which interacts with the separable phase is placed so as to cause drift of that phase in the direction parallel to the narrow dimension of the flow channel. The field-induced drift causes the separable phase to concentrate, at steady state, along one of the broad faces of the channel in a roughly exponential profile, whose characteristic exponential distance is given by $D/U$, where $D$ is the diffusivity of the separable phase in the surrounding solvent and $U$ is the field-induced average drift velocity of the separable phase. The flow in the channel is assumed to be laminar, and therefore the separable phase is transported down the channel at different velocities, depending upon the velocity of the solvent at the position of the concentrated separable phase. Demonstrations of this technique using gravitational, centrifugal, electrical, magnetic, cross-flow, thermal, and chemical fields have been published (*8*).



In all of the following, we consider slow flow in a channel of circular cross-section of radius $R$. The particle density is assumed small enough so that the fluid viscosity is not affected. The velocity of the fluid at radius $r$ is given in the absence of particles by

$$v_f(r) = 2\langle V\rangle(R^2 - r^2)/R^2 \tag{1}$$

where $\langle V\rangle$ is the average flow velocity.

The interaction of particles and the carrier fluid can yield unexpected effects in laminar flow. In the first place, a particle does not move downstream (chosen to be the $z$-direction) at the velocity of the streamline at its center (*9*). In the absence of all other effects, particles lag behind the surrounding fluid with the difference in longitudinal velocity, $\Delta v_z$, between the fluid at the position of the center of the particle and the particle itself, given approximately by (*10*, *11*)

$$\Delta v_z \approx \langle V\rangle(d_p/R)^2/6 \tag{2}$$

where $d_p$ is the diameter of the particle, and $d_p \ll R$.

This relative velocity between fluid and particle can be significantly modified if the flow direction is vertical and the particle is not neutrally buoyant. In that case, $\Delta v_z$ must be augmented or diminished by the Stokes settling velocity,

$$v_g = d_p^2 g \Delta\rho / 18\mu \tag{3}$$

depending on the sense of flow, where $g$ is the acceleration of gravity, $\Delta\rho$ is the difference in density between the particle, $\rho_p$, and the fluid, $\rho_f$, and $\mu$ is the viscosity of the fluid.

The relative longitudinal velocity between fluid and particle gives rise to a force on the particle in the radial direction. This effect, discussed initially by Saffman (*12*), forces particles toward the center of the tube if the particles lag the fluid, and toward the tube walls if the particles lead the fluid. The force increases with the square root of the radial position of the particle, $r_p$. Applying the Stokes coefficient to the Saffman force leads to the following expression for the radial velocity component attributable to this effect:

$$v_{Sr}(r_p) = -0.3427 \Delta v_z (r^* \mathrm{Re})^{1/2} d_p / R \tag{4}$$

where $r^* = r_p/R$, the normalized particle radial position, and where Re is the tube Reynolds number, given by $\mathrm{Re} = \rho_f \langle V \rangle R/\mu$. In the event that $\Delta v_z$ is given by Eq. (2), which is appropriate for flow in a horizontal tube, the Saffman velocity is given by

$$v_{Sr}(r_p) = -0.0571 \langle V \rangle (r^* \mathrm{Re})^{1/2} (d_p/R)^3 \tag{5}$$

Yet another transverse force has been noted. This force, investigated experimentally by Segré and Silberberg (*13*) and Aoki et al. (*14*), was described theoretically by Ho and Leal for plane flows (*15*). The force depends on the square of the flow velocity, and in a cylindrical flow tube the force is positive (toward increasing radius) for $r_p$ less than about $0.6R$, and negative for $r_p$ greater than that value. Thus, the Ho and Leal effect pushes particles toward a thin annular region of the tube at a radius of about $0.6R$. Aoki called this the tubular pinch effect.

In the absence of an expression for the Ho and Leal force in Hagen-Poiseuille flow, we adapt Ho and Leal's expression (*15*) for this transverse force from that given for the plane Poiseuille flow situation. In our adaptation we imagine the fluid velocity distribution to have the same

maximum at the center of both the plane and cylindrical channels, $V_{max}$. In the plane flow case, the average flow velocity is equal to $2V_{max}/3$. In our cylindrical case, $\langle V \rangle = V_{max}/2$. This difference in the definition of the average velocity requires that the Ho and Leal expression be modified by a factor of $(4/3)^2$. This modification maintains the transverse shear field but neglects the curvature of the streamlines. It leads to an approximate radial velocity attributable to this force given by

$$v_{Hr}(r_p) = -0.106\langle V \rangle \mathrm{Re}(d_p/R)^3 H(r^*) \tag{6a}$$

where

$$H(r^*) = r^*(G_1 r^* - G_2) \tag{6b}$$

$G_1$ and $G_2$ are themselves functions of $r^*$, and were tabulated by Ho and Leal (*15*). The function $H(r^*)$ is shown in Fig. 1. $H(0) = 0$, an unstable point for a particle, and $H(r^*) < 0$ until $r^* = G_2/G_1$. This occurs at approximately $r^* = 0.6$. For larger arguments, $H(r^*) > 0$.

When a flow tube is placed horizontally, particles carried by the fluid in this tube will be moved in the radial direction by both $v_{Sr}$ and $v_{Hr}$. In addition, they will rise or fall vertically in the tube according to the Stokes

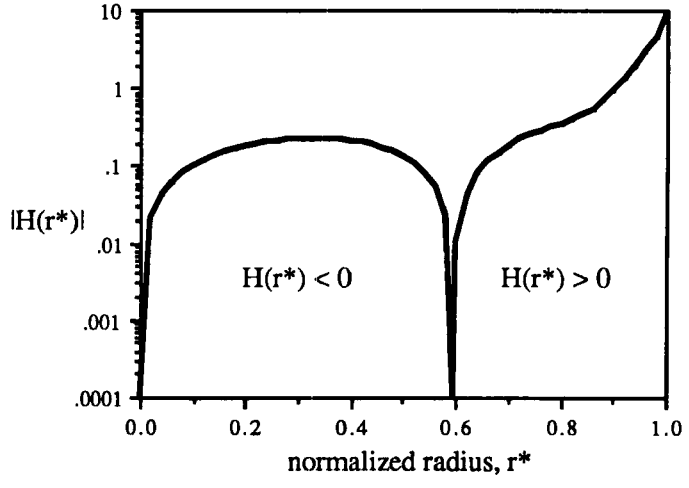


FIG. 1. The magnitude of the function $H(r^*)$ as a function of the normalized tube radius, $r^*$. See Eqs. (6a) and (6b) in text.

settling velocity. Within a certain range of system parameters, if the particles are denser than the fluid, and if the combined $S$ and $H$ forces are strong enough to overcome gravity, the particles will be pinched into a narrow crescent region below the center of the tube at $r^* > 0.6$, ultimately arriving at an equilibrium normalized radius, $r_\infty$, directly below the tube center. Particles lighter than the fluid will rise to a point above the tube center in a similar way. Particles so trapped at $r_\infty$ will be transported longitudinally down the tube at the stream velocity less $\Delta v_z$, that is,

$$v_{pz}(r_\infty) = 2\langle V\rangle(1 - r_\infty^2) - \Delta v_z \tag{7}$$

Particles unable to be trapped will eventually be forced against the tube wall.

In contrast to the theory of FFF, we do not explicitly include the effects of diffusion caused by Brownian motion of the particles. We limit our investigation to large particles for which the diffusive velocity is negligible compared to the cross-flow velocities introduced above.



## DISCUSSION

With regard to the geometry of the flow tube shown in Fig. 2, it is clear that the velocity of a particle $\mathbf{v}_p = (v_{px}, v_{py}, v_{pz})$ is a function of its position $(x_p, y_p)$ within the cross section of the flow tube. Thus, from the equations provided above,

$$v_{px} = v_r(r_p)x_p/r_p \tag{8a}$$

$$v_{py} = v_r(r_p)y_p/r_p - v_g \tag{8b}$$

and

$$v_{pz} = 2\langle V\rangle(1 - r^{*2}) - \Delta v_z \tag{8c}$$

where

$$v_r(r_p) = v_{Sr}(r_p) + v_{Hr}(r_p)$$

and

$$r_p = (x_p^2 + y_p^2)^{1/2}$$

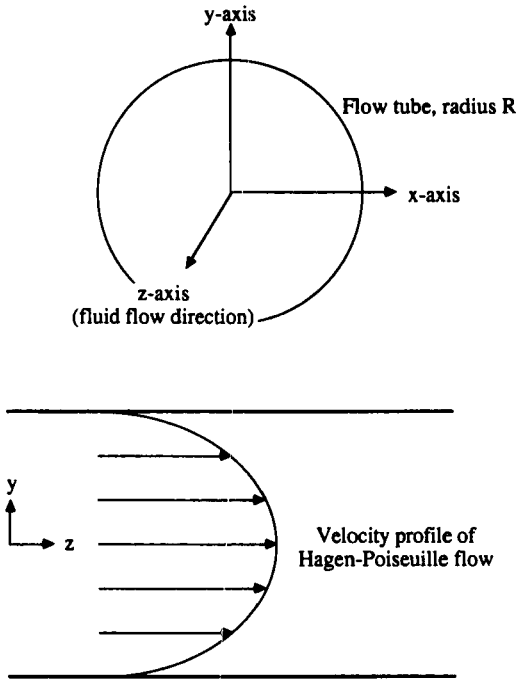


FIG. 2. Geometry of the flow tube.



Given any initial position of a particle, say $\mathbf{x}_0 = (x_0, y_0, z_0)$, the trajectory of the particle is obtainable in principle by integration:

$$\mathbf{x}(t) = \int \mathbf{v}_p dt + \mathbf{x}_0$$

The complexity of these equations precludes their integration in closed form. Thus, we have integrated them digitally. We seek the time, $T$, at which a particle initially positioned randomly within the cross section of the tube at $z = 0$ will travel a distance $L$ down the tube. The particle is constrained to remain entirely within the tube, therefore $r_p \leqslant R - d_p/2$. As $T$ will vary with initial position, we generated a histogram of arrival times for particles whose initial positions were uniformly distributed across the $z = 0$ plane. Particles were placed initially on a grid with spacing $R/10$, the grid being offset $R/20$ in both the $x$ and $y$ directions from the center of the tube. This grid yields 316 starting points within the cylinder on the

$z = 0$ plane, of which only 158 give unique results due to left-right symmetry. Figure 3 shows an example of this histogram of arrival times. The parameters used in this calculation are $R = 0.0381$ cm, $L = 231.5$ cm, $\mu = 0.01018$ P, $\rho_f = 1.0046$ g/cm$^3$, $\rho_p = 1.05$ g/cm$^3$, and $\langle V \rangle = 4.56$ cm/s. Arrival times are shown for particles of diameters 40, 50, 60, 70, 80, 90, and 100 μm. We note that the larger particles arrive earlier, and with a narrower distribution compared to the smaller particles. The ordinate of the distribution plot is in units of % of particles arriving per ¼-s time interval. Due to the finite number of particles used in our simulation, the distributions are not smooth. However, we have calculated the mean arrival time ($\langle T \rangle$) and the standard deviation ($\Delta T_c$) as a function of particle diameter. These results are shown in Figs. 4 and 5. The data points shown on these figures will be discussed in the following section.

In order to gain insight into this behavior, we note that the trajectory of a particle consists of two phases. In the first phase, the particle moves transverse to the flow from its initial position to either $r_\infty$ or to the tube wall while at the same time moving downstream at velocities determined by the particle's instantaneous radial position. In the second phase, the particle is carried downstream at the constant velocity given by Eq. (8c) with $r^* = r_\infty$ for trapped particles and $r^* = 1 - (d_p/2R)$ for particles forced against the wall of the cylinder. Some particles never achieve the second



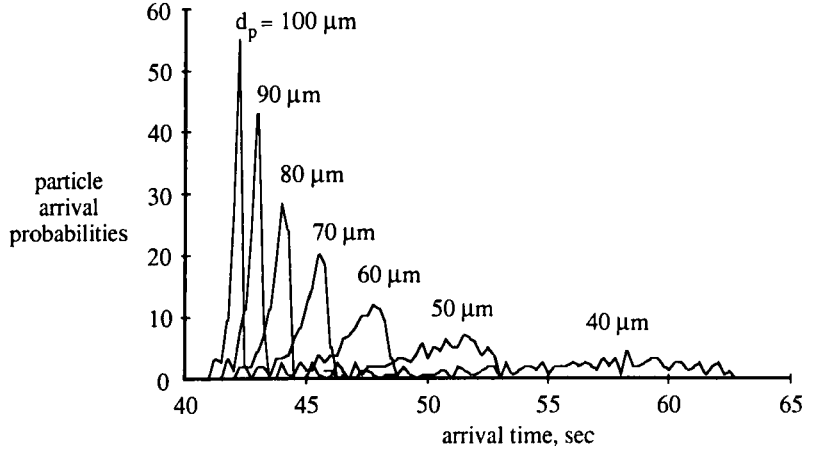


FIG. 3. Calculated arrival distributions for spherical particles of different diameters, $d_p$. The flow system parameters are given in the text.

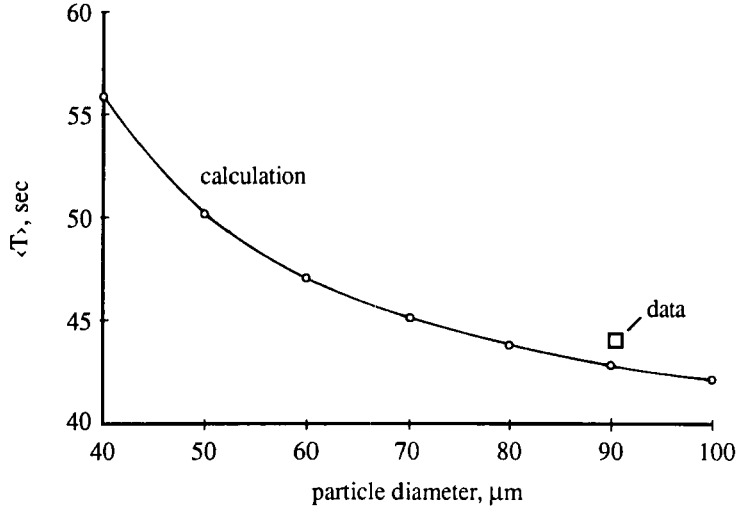


FIG. 4. Mean arrival times, $\langle T \rangle$, for arrival distributions shown in Fig. 3. The data point shows the mean arrival time for polystyrene particles in a flow system described by the given system parameters. The mean diameter of the particles was 90.7 μm according to the manufacturer.

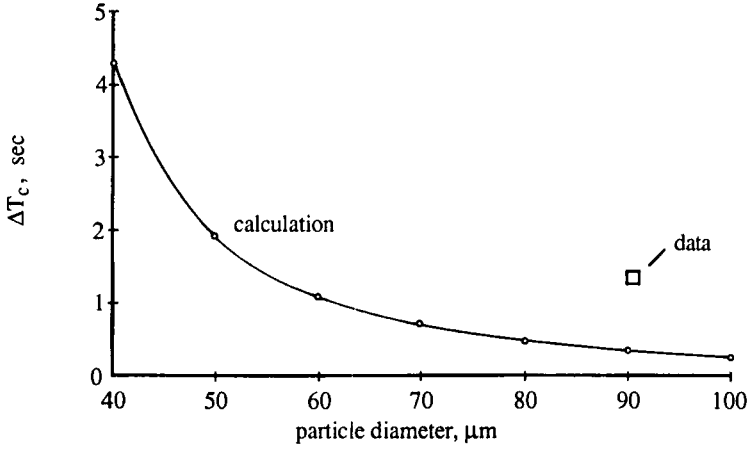


FIG. 5. Calculated standard deviations, $\Delta T_c$, of the particle arrival distributions shown in Fig. 3. The data point shows the measured standard deviation, $\Delta T_m$, of the arrival distribution for our 90.7 μm particles.

phase. This latter situation occurs if the combined transverse velocity components given by Eqs. (8a) and (8b) are so small that the particle doesn't reach its final radial position before the particle passes $z = L$. If the majority of the particles initially distributed uniformly across the $(x, y, 0)$ plane never reach the second phase of their trajectory, then the arrival distribution will be very broad, approximating the arrival function of the carrier fluid itself (*16*).

For Re > 1, the Ho and Leal force exceeds the Saffman force for $r^* > 0.6$. Therefore, neglecting the Saffman velocity, we can write an approximate relationship derived by setting Eq. (8b) equal to zero for a particle which has come to its equilibrium radial position along the $y$-axis:

$$H(r_\infty) \cong \frac{g\left(\frac{|\Delta\rho|}{\rho_f}\right)R^2}{1.908\langle V\rangle^2 d_p} \tag{9}$$

If the right side of this equation is less than about 10, a value of $r_\infty$ may be found by reference to Fig. 1. If $r_\infty < 1 - (d_p/2R)$, then the particle will be trapped by the tubular pinch effect. If the inequality does not hold, or if a solution to Eq. (9) cannot be found, then the particle is forced to the wall of the tube.

Equation (9) shows that larger particle diameters lead to smaller values of $H(r_\infty)$, which are satisfied by values of $r_\infty$ closer to 0.6. The downstream velocity is greater at smaller tube radii, therefore larger particles have a larger downstream velocity once they achieve the second phase of their trajectory.

The time necessary to complete the first phase of the trajectory is smaller for particles having larger Stokes settling velocity, $v_g$. Thus, for particles of a given density, larger particles settle first, and achieve phase two more quickly than smaller particles. This affects the width of the arrival distribution function, since for particles having different initial positions, the variable distance traveled downstream during phase one causes the variance in the arrival distribution in the first place.

One can vary any of the parameters and calculate the resulting arrival distributions. One of these possibilities is shown in Fig. 6, where the values for $R$, $L$, $\mu$, $\rho_f$, and $\rho_p$ are the same as given above, $d_p$ is set equal to 90.7 μm, and we have chosen $\langle V\rangle$ equal to 3, 3.5, 4, 4.5, and 5 cm/s. The mean arrival times for these distributions are shown in Fig. 7.

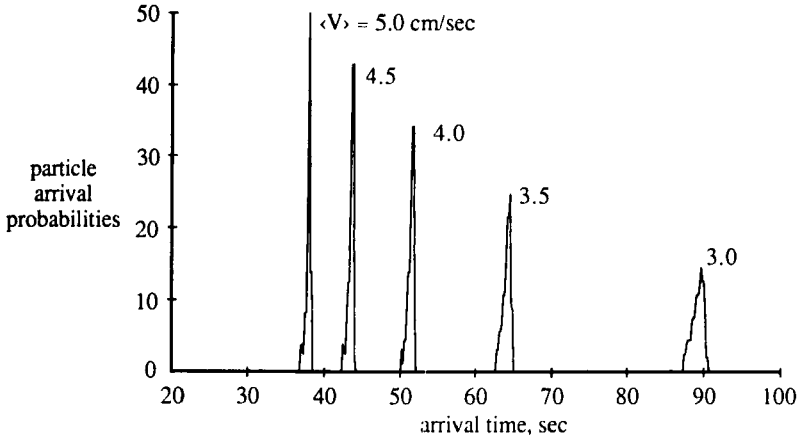


FIG. 6. Calculated arrival distributions for 90.7 μm particles for different average flow velocities. All other system parameters remain the same.



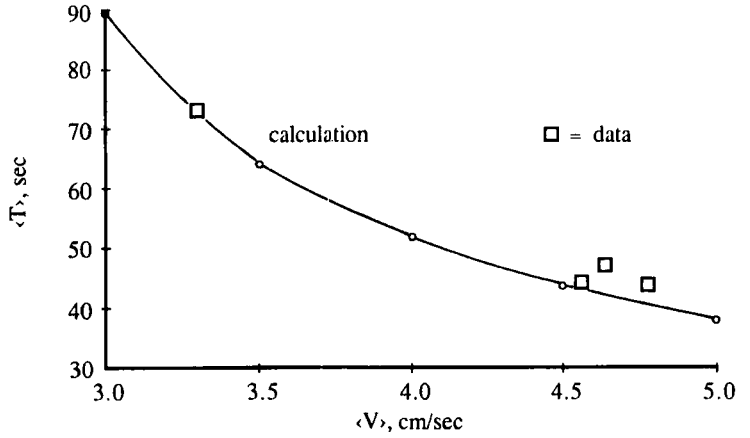


FIG. 7. Mean arrival times, $\langle T \rangle$, for particle distributions shown in Fig. 6. The data points show the measured mean arrival times for our 90.7 μm polystyrene particles at the indicated average flow velocities.

## EXPERIMENTAL RESULTS

Pinch field-flow fractionation experiments were conducted in an apparatus shown schematically in Fig. 8. A carrier fluid consisting of 0.9% saline was forced through a substantially horizontal coil of Tygon microbore tubing with an inner diameter of 0.762 mm. The flow system was held at constant temperature in a water bath. A constant pressure drive for the carrier fluid was arranged using a pressurized vessel. Samples of polystyrene spheres of approximately 10% by volume were prepared in similar saline fluid, with the addition of a small amount of detergent. These samples were injected into the flow system using a tandem arrangement of solenoid pinch valves operating on silicone pinch tubing, which controlled the flow of sample and carrier stream through a "π"-shaped injector valve. The injector fitting was machined from a small block of clear acrylic plastic, and upon activation of the solenoids, a constant sample volume of approximately 5 μL was injected into the flow system.

The particle sensor was placed 231.5 cm down the tube, and consisted of a simple ac impedance cell. A frequency of 50 kHz was used, and the change in resistance of the fluid moving through the cell was recorded as a function of time after sample injection, using a lock-in amplifier to pick out the in-phase component of the impedance, and a chart recorder. When the cell contained a volume of the nonconducting particles, an increased resistance was measured compared to that of the carrier fluid.



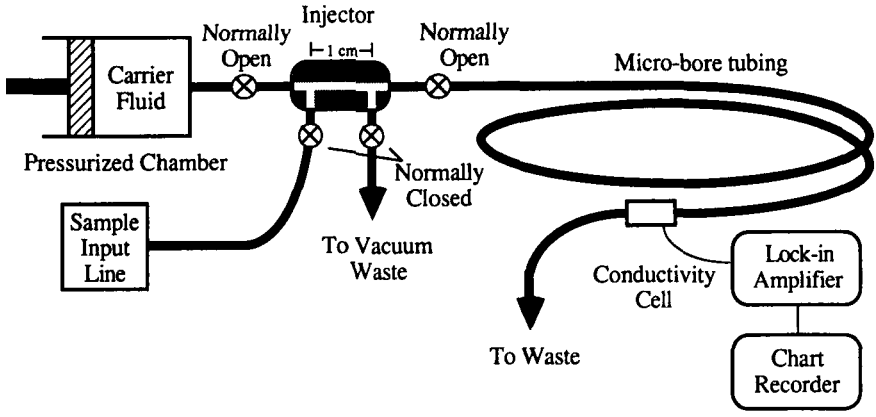


FIG. 8. Schematic diagram of experimental system.

Changes in cell resistance on the order of 0.005%, corresponding to less than 0.1% solids, were routinely measured by this system.

Figure 9 shows a typical signal (solid curve) from our apparatus, after injection of a sample containing polystyrene spheres characterized by the manufacturer as having a mean diameter of 90.7 μm. The mean fluid velocity was 4.56 cm/s. The signal pulse shown in Fig. 9 is accompanied by two calculated particle arrival distributions (dotted curves) reproduced from Fig. 3, one for 100 μm particles and the second for 80 μm particles. The three curves have been normalized to the same area. Note that the parameters used to calculate the distributions shown in Fig. 9 correspond to the experimental situation described above.

The experimental signal in Fig. 9 indicates a mean particle arrival time of 43.9 s, which is also shown as the data point on Fig. 4. We note that the measured mean arrival time is fairly close to that predicted from our theory for 90.7 μm particles. A variation in any one of the many system parameters, or a slight timing error on our chart recorder could be responsible for the observed 2.5% discrepancy between measured and predicted arrival times. The data points in Fig. 7 show measured mean arrival times for these 90.7 μm particles in the same system at different values of $\langle V \rangle$. There is quite a good correspondence between experiment and theory.

Another interesting observation is the fact that the width of the signal



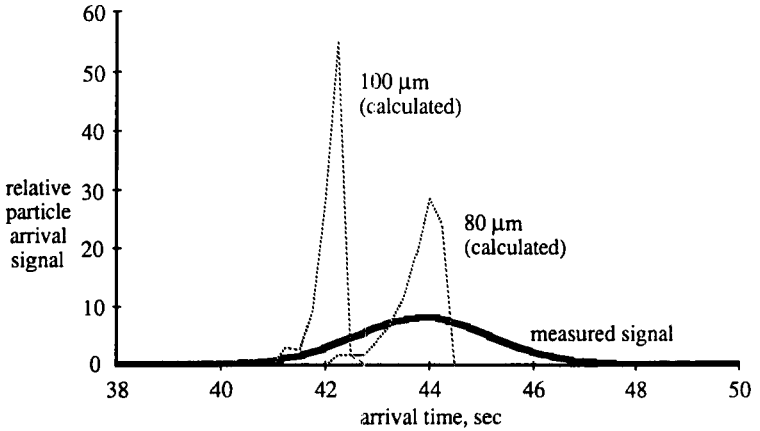


FIG. 9. Measured arrival distribution (solid curve) for 90.7 μm particles with calculated arrival distributions for particles of 100 and 80 μm. All the curves were normalized to equal area, and the system parameters reflect the experimental situation.

pulse is much larger than expected for particles of this size. Figure 5 shows the measured standard deviation of the signal pulse ($\Delta T_m$ = 1.27 s) obtained at $\langle V \rangle$ = 4.56 cm/s for 90.7 μm particles superimposed on the calculated standard deviation of the arrival time distribution for this experimental situation. Analysis of this discrepancy follows.

## ANALYSIS OF SIGNAL PULSE WIDTH

The variance (square of the standard deviation) of a measured signal pulse is caused by three factors. The first is the intrinsic variance which results when particles of the same size, but distributed initally in a uniform fashion across the $(x, y, 0)$ plane of the flow tube, settle down to $r_\infty$ at different times, thereby arriving at $z = L$ with a characteristic arrival width. This intrinsic component of the arrival distribution width was calculated previously, and is shown in Fig. 5. For the experimental situation under consideration, with $d_p$ = 90.7 μm, $\Delta T_c$ = 0.33 s.

The second contribution to the variance of the measured signal results from the fact that the sample pulse is in reality a slug of uniformly distributed particles in carrier fluid, occupying an initial length of $\Delta L$ = 1 cm in the flow tube. Thus, the effective length of the tube from sample injection point to sensor varies from $L$ to $L + \Delta L$ for the various particles in the sample. This effect can be accommodated fairly simply by defining a second contribution to the width of the measured signal pulse, $\Delta T_L$, proportional to $\Delta L$ divided by the average particle velocity. Since a square pulse has a second moment or variance given by the square of the pulse width divided by 12, we find $\Delta T_L = (\Delta L/\sqrt{12})/(L/\langle T \rangle)$. In our case, $\Delta T_L$ = 0.055 s.

The last contribution to the variance of the measured signal results from the distribution of particle size in the sample itself. Figure 4 shows when particles of different diameters are expected to arrive at the sensor. If the particles of the sample have a standard deviation of $\Delta d_p$, then this would cause a broadening in the arrival time pulse given by $\Delta T_d = \Delta d_p \partial(\langle T \rangle)/\partial(d_p)$. The slope of the $\langle T \rangle$ vs $d_p$ curve in Fig. 4, evaluated at $d_p$ = 90.7 μm is $\partial(\langle T \rangle)/\partial(d_p)$ = 0.084 s/μm.

As these three contributions to pulse width are independent, we use the familiar law that the variance of a random process is given by the sum of the variances contributed by the components of the process. Thus,

$$\Delta T_m^2 = \Delta T_c^2 + \Delta T_L^2 + \Delta T_d^2 \tag{10}$$

By using Eq. (10) and the values given above, we can solve for the standard deviation of our particle size distribution. Thus,

$$\Delta d_p = (\Delta T_m^2 - \Delta T_c^2 - \Delta T_L^2)^{1/2}/[\partial(\langle T \rangle)/\partial(d_p)] \qquad (11)$$

which gives $\Delta d_p = 14.6$ μm. The standard deviation of the diameter of the 90.7 μm particles quoted by the manufacturer is 14.5 μm.

## CONCLUSIONS

The theory presented for the pinch field-flow fractionation mechanism agrees very well with our experimental findings. We note that the theory presented contains no fitting factors, but uses only the parameters of the flow system itself. The theory not only accurately predicts the arrival time of particles, but also permits the width of the arrival signal to be related to the particle size distribution.

By varying the system parameters, including carrier fluid density, average flow velocity, and size of tubing, one can design a fractionation apparatus to work successfully over a wide range of particle sizes and densities. This mechanism permits fractionation of particles comparable to those shown separable using steric FFF techniques. An advantage of this method is that fractionation occurs more rapidly than with steric FFF since particles are not forced to the lowest flow velocity regions of the flow tube, but are instead pinched into a high velocity streamline by the fluid forces developed in the Hagen-Poiseuille flow tube. In addition, the apparatus is significantly simpler, since high transverse fields need not be employed, and in fact may be implemented with a standard flow injection analysis (FIA) system.

A recent study of heterogeneous samples (e.g., whole blood) in FIA systems (*17*) has shown that significant errors in chemical analysis can be made because reproducible dispersion is not maintained due to the effects of the cells. We suggest that to the extent that red blood cells can be modeled as rigid spheres, the theory presented herein could be developed into useful techniques for measuring and correcting for variations in hematocrit, or determining cell size distributions with very small samples in FIA systems.



### Acknowledgments

The authors gratefully acknowledge the support of the Center for Process Analytical Chemistry at the University of Washington, and thank Professor J. Ruzicka for stimulating discussion.

## REFERENCES


1. J. C. Giddings, "A New Separation Concept Based on a Coupling of Concentration and Flow Nonuniformities," *Sep Sci., 1*(1), 123-125 (1966).
2. J. C. Giddings and M. N. Myers, "Steric Field-Flow Fractionation: A New Method for Separating 1 to 100 μm Particles," *Sep. Sci. Technol., 13*(8), 637-645 (1978).
3. R. E. Peterson, II, M. N. Myers, and J. C. Giddings, "Characterization of Steric Field-Flow Fractionation Using Particles to 100 μm Diameter," *Ibid., 19*(4&5), 307-319 (1984).
4. T. Koch and J. C. Giddings, "High-Speed Separation of Large (>1 μm) Particles by Steric Field-Flow Fractionation," *Anal. Chem., 58,* 994-997 (1986).
5. K. D. Caldwell, T. T. Nguyen, M. N. Marcus, and J. C. Giddings, "Observations on Anomalous Retention in Steric Field-Flow Fractionation," *Sep. Sci. Technol., 14*(10), 935-946 (1979).
6. D. F. McTigue, R. C. Gilver, and J. W. Nunziato, "Rheological Effects of Nonuniform Particle Distributions in Dilute Suspensions," *J. Rheol., 30*(5), 1053-1076 (1986).
7. J. Ruzicka and E. H. Hansen, *Flow Injection Analysis,* Wiley, New York, 1981.
8. E. Grushka, K. D. Caldwell, M. N. Myers, and J. C. Giddings, "Field Flow Fractionation," *Sep. Purif. Methods, 2*(1), 127-151 (1973), and references therein.
9. H. Brenner, "Hydrodynamic Resistance of Particles at Small Reynolds Numbers," *Adv. Chem. Eng., 6,* 287-438 (1966).
10. R. Simha, *Kolloid Z., 76,* 16 (1936).
11. J. Happel and B. J. Byrne, "Motion of a Sphere and Fluid in a Cylindrical Tube," *Ind. Eng. Chem., 46*(6), 1181-1186 (1954).
12. P. G. Saffman, "The Lift on a Small Sphere in a Slow Shear Flow," *J. Fluid Mech., 22*(2), 385-400 (1965); corrigendum: *31,* 624 (1968).
13. G. Segré and A. Silberberg, "Behaviour of Macroscopic Rigid Spheres in Poiseuille Flow. Part 1," *Ibid., 14,* 115-135 (1962); G. Segré and A. Silberberg, "Behaviour of Macroscopic Rigid Spheres in Poiseuille Flow. Part 2," *Ibid., 14,* 136-157 (1962).
14. H. Aoki, Y. Kurosaki, and H. Anzai, "Study of the Tubular Pinch Effect in a Pipe Flow," *Bull. JSME, 22*(164), 206-212 (1979).
15. B. P. Ho and L. G. Leal, "Inertial Migration of Rigid Spheres in Two-Dimensional Unidirectional Flows," *J. Fluid Mech., 65*(2), 365-400 (1974).
16. P. V. Danckwerts, "Continuous Flow Systems," *Chem. Eng. Sci., 2*(1), 1-13 (1953).
17. J. J. Harrow and J. Janata, "Heterogeneous Samples in Flow-Injection Systems; Part 1. Whole Blood," *Anal. Chim. Acta, 174,* 115-122 (1985).


*Received by editor March 7, 1988*
*Revised July 27, 1988*